Journal of Manufacturing Processes 148 (2025) 224–236

Contents lists available at ScienceDirect

Journal of Manufacturing Processes

journal homepage: www.elsevier.com/locate/manpro

Feature-oriented vibrations in LCD-based vat photopolymerization

Han Xu [a,b], Qizhou Li [a,b], Shangxiong Zhang [a,b], Changyuan Pu [a,b], Yizhu Chen [a,b], Yong Chen [a,b,c,d,*]

[a] Center for Advanced Manufacturing, University of Southern California, Los Angeles, CA 90007, USA
[b] Department of Aerospace and Mechanical Engineering, University of Southern California, Los Angeles, CA 90089, USA
[c] Department of Industrial and Systems Engineering, University of Southern California, Los Angeles, CA 90089, USA
[d] Department of Biomedical Engineering, University of Southern California, Los Angeles, CA 90089, USA

ARTICLE INFO

Keywords:
Additive manufacturing
Vat photopolymerization
Piezo vibration
Aliasing
Liquid crystal display

ABSTRACT

Liquid crystal display (LCD)-based vat photopolymerization (VPP) is a versatile and accessible 3D printing technology due to its low cost and fast printing speed. It is ideal for applications requiring rapid fabrication of high-resolution intricate geometry. However, as the feature size approaches the resolution limit (a single pixel) of the LCD mask, undesirable pixelated aliasing emerges, resulting in increased roughness and dimensional inaccuracies. This study introduces a new feature-oriented vibration method in LCD-based VPP to enhance linear feature fabrication precision. Coupled with grayscale mask images, it can significantly reduce pixelated aliasing and improve dimensional accuracy in printing linear features. In this method, the mask images are vibrated along the direction of a linear feature to enhance its feature smoothness while maintaining dimensional accuracy. The vibration amplitude is optimized based on the simulation of the printing results derived from the light energy model of the LCD mask. This method achieves up to a 4× improvement in line roughness (0.6 μm–1.5 μm) compared to conventional vat photopolymerization (1.2 μm–5.9 μm) and demonstrates precise dimensional control with subpixel-level (10 μm) accuracy for an LCD with 50 μm pixel size. The advantages of the feature-oriented vibration method are further highlighted through the fabrication of honeycomb metamaterials with enhanced strength and micro-filters with customizable shapes and mesh sizes. The study demonstrates that controlled vibrations provide an effective path for future VPP development in microstructure fabrication.

1. Introduction

The increasing demand for fabricating high-resolution and intricate geometry has driven extensive research and development in additive manufacturing (AM). For example, the cellular structure of wood characterized by tube-like thin-line geometries (Fig. 1a) achieves remarkable strength while maintaining a lightweight profile [1], highlighting the potential of complex micro-architectures enabled by AM. Among AM technologies, vat photopolymerization (VPP) has emerged as a fabrication method that offers microscale accuracy [2–4], rapid fabrication speed [5,6], and adequate strength and stiffness [7,8]. These attributes have facilitated its widespread commercialization, enabling high-resolution applications across diverse industries. The laser-based and digital micromirror device (DMD)-based VPP has been employed in the production of customizable dental crowns and aligners, biocompatible implants, and metamaterials with intricate multi-scale features [9–14]. In recent years, the liquid crystal display (LCD)-based VPP has gained significant popularity due to its affordability and scalability, offering a cost-effective alternative for desktop 3D printing systems. However, advancements in LCD-based VPP technology are still needed to close the performance gap compared to the DMD-based VPP systems for industrial applications.

The LCD-based VPP's resolution is determined by the resolution of the mask images (20 μm–50 μm) and the layer thickness (10 μm–200 μm) [15,16]. When the printed feature size approaches the resolution limit of the LCD's mask image, a common issue arises in pixelated aliasing [17]. Pixelated aliasing manifests as zigzag textures on the surfaces or boundaries of 3D-printed objects. This issue stems from the discrete structure of the LCD screen used as the photomask in the 3D printing process [18]. That is, when photomask images are used to define curves or diagonal lines, the system approximates smooth shapes by aligning them with a grid of pixels. Consequently, the approximation error leads to dimensional deviations and rough boundaries on the 3D-printed results (Fig. 1b-left). Eliminating pixelated aliasing is essential

* Corresponding author at: Center for Advanced Manufacturing, University of Southern California, Los Angeles, CA 90007, USA.
E-mail address: yongchen@usc.edu (Y. Chen).

https://doi.org/10.1016/j.jmapro.2025.05.034
Received 23 February 2025; Received in revised form 1 May 2025; Accepted 18 May 2025
Available online 22 May 2025

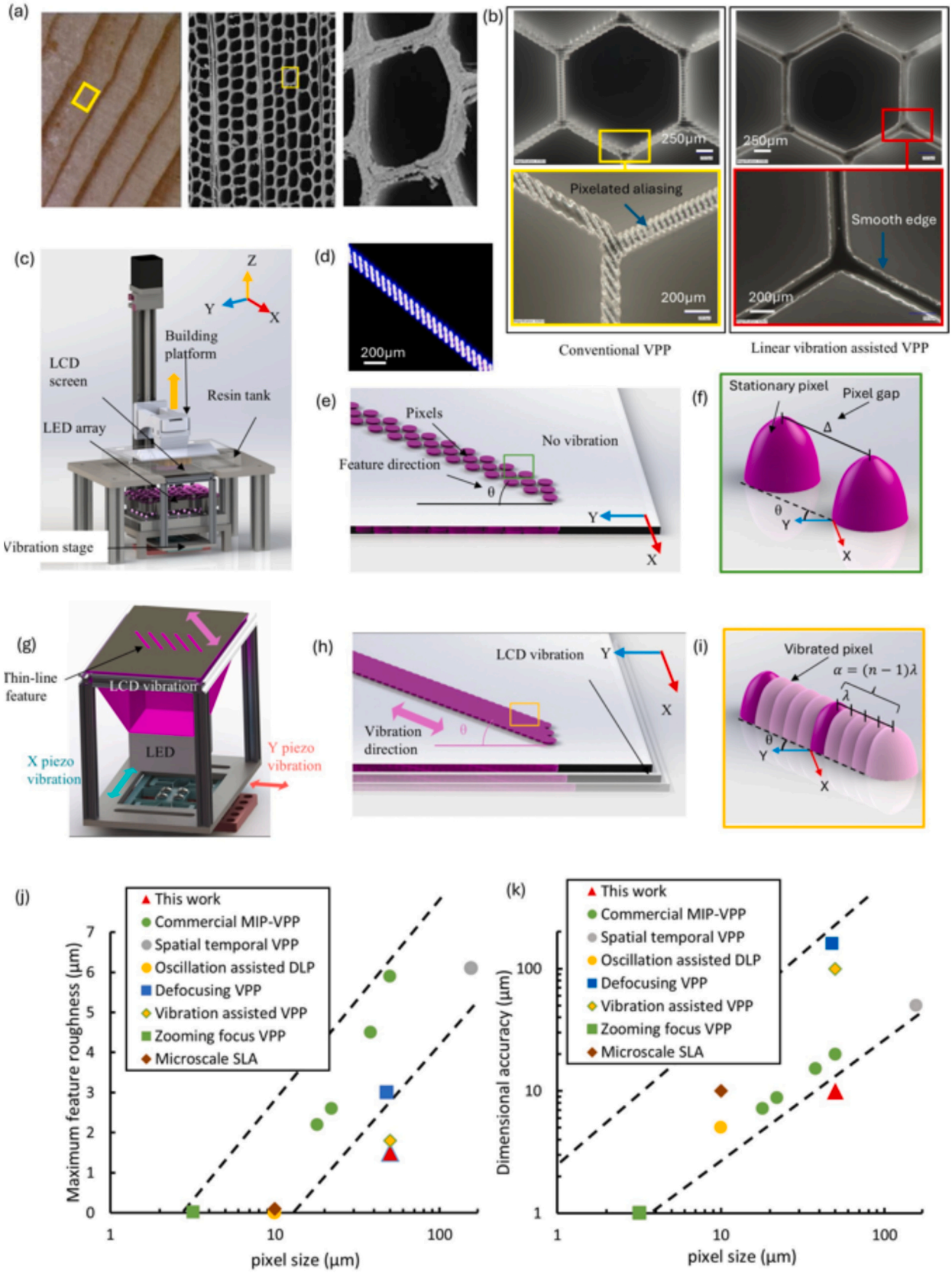

Fig. 1. Introduction of the LFV-VPP process. (a) Cross section of wood, and wood cells, reproduced with permission [1]; (b) 3D-printed honeycombs using a commercial LCD-based VPP system and LFV-VPP; (c) schematic of an LFV-VPP printer; (d) a mask image of a thin line feature; (e) schematic of pixelated aliasing in the thin line feature; (f) schematic of two neighboring pixels in the thin line feature; (g) schematic of mask image vibration along the line direction; (h) schematic of the vibrated thin line feature with smooth boundary; (i) effect of the linear feature-oriented vibration on two neighboring pixels; (j) a summary of existing VPP processes in the literature regarding feature smoothness over pixel size; and (k) a summary of existing VPP processes regarding the dimensional accuracy over pixel size.

for high-accuracy fabrication of microscale geometries for future LCD-based VPP technology.

1.1. Related works

Several approaches have been developed to address pixelated aliasing in the DMD-based VPP [17,19–22]. Recently, spatial-temporal VPP was invented to improve pixel resolution by splitting each pixel into multiple subpixels [23]. Oscillation-assisted digital light processing was developed by adding a vibrator to the objective lens of the DLP projector to homogenize light intensity variations in mask images [24]. One significant difference between the DMD-based and LCD-based VPP is that the DMD-based VPP has an integrated optical system to adjust the focus of the mask image so the desired pixel blending between neighboring pixels can be achieved [25]. In comparison, LCD-based 3D printers usually use a direct contact configuration, in which the LCD screen directly contacts the building platform through a thin separation film, e.g., a fluorinated ethylene propylene (FEP) film. Hence, pixelated aliasing defects are more evident in the LCD-based VPP since less pixel blending between neighboring pixels exist in the direct contact configuration.

Due to a shorter development period, less previous work has been found on addressing pixelated aliasing in the LCD-based VPP. Defocus mask image projection-based VPP introduces a physical separation between the LCD screen and the liquid resin, utilizing light scattering to introduce pixel blending between neighboring pixels and reduce pixelated aliasing [18]. However, it reduces the printing resolution and accuracy. Recently, a general vibration-assisted VPP method was presented to reduce pixelated aliasing in the LCD-based VPP by vibrating the mask image in the *XY* plane within a one-pixel amplitude [26]. This feature-independent vibration method can reduce pixelated aliasing caused by light intensity variations to achieve smooth surface fabrication; however, it also introduces additional geometric errors and distorts the printed thin features. Inspired by this vibration-integrated work, we aim to develop a new vibration method in LCD-based VPP that can effectively eliminate linear features' pixelated aliasing defects at the sub-pixel level without compromising their dimensional accuracy.

1.2. Contributions

We present a Linear Feature-oriented Vibration (LFV) method for the LCD-based VPP, named LFV-VPP, to reduce its pixelated aliasing defects. This method vibrates the photomask along the direction of a linear feature, improving the linear feature's smoothness without sacrificing dimensional accuracy. To validate this concept, we developed an in-house-built LFV-VPP 3D printer (Fig. 1c) with an LCD screen capable of moving in arbitrary directions within the *XY* plane using piezo-based linear stages (Fig. 1g). The feature-oriented vibration of the LCD screen blends the pixels in the vibration direction, turning the jagged line features into smooth, continuous features (Fig. 1h). We investigated optimal vibration amplitude α to achieve the desired smoothness (Fig. 1i). A convoluted ultraviolet (UV) energy model of LCD photomask images has been established to predict the fabrication results, optimizing the line width and smoothness. To demonstrate the benefits of this approach, we built microscale honeycomb structures with smooth cellular walls (Fig. 1b-right), which exhibited reduced stress concentrations and enhanced maximum compressive strength (refer to Video S1 in Support Information). We also fabricated customized mesh filters to test subpixel-level control over feature dimensions for micro-particle filtering (refer to Video S2 in Support Information). The LFV-VPP reduced feature roughness to a range of 0.6 μm to 1.5 μm for line features oriented in arbitrary directions. Compared to existing approaches, the LFV-VPP technique achieved the highest roughness for the same 50 μm pixel size (Fig. 1j — refer to Table S1 in Support Information). It also demonstrated superior control over dimensional accuracy, with deviations controlled within 10 μm for the 50 μm pixel size. This accuracy surpasses defocusing VPP or feature-independent vibration VPP processes (Fig. 1k).

2. Material and methods

2.1. Vat photopolymerization material

Standard commercial resin in clear color, supplied by AnyCubic Technology Co., Ltd., was utilized in all the experiments. The material was used as received without any modifications. The curing depth of the resin was calibrated by printing single-layer thin sheets using an AnyCubic Mars 2 Pro 3D printer. The relationship between the curing depth of the selected material and the accumulated UV energy is illustrated in Fig. S1. The tensile strength of the resin is 40–50 MPa, and the elongation at break is 12–16 % [27].

2.2. A 3D printer based on LFV-VPP

An LCD-based VPP integrated with a piezo-based linear motion system, developed in our previous work [26], was adopted with revised vibration control in this study (Fig. 1c). The printer utilizes two piezo actuators (PC4QQ, 18.0 μm max displacement, size 6.5 mm × 6.5 mm × 18.0 mm) to move an LCD screen-embedded structure in the *XY*-plane. Two in-house developed vibration amplifiers were employed to increase the maximum displacement of the piezo actuators from 18.0 μm to 90.0 μm. The system achieves a 5 μm resolution in *XY* movement in microseconds using the piezo actuators. The LCD screen, a 5.5-inch monochrome Mars 2 Pro from Elegoo™, was used to generate dynamic photomask images, with a resolution of 1440 × 2560 pixels and a nominal pixel size of 50 μm. A 405 nm UV light-emitting diode (LED) array from Shenzhen Aptus Technology Co., Ltd. was used as the light source for photocuring liquid resins. A 150 μm thick FEP film from Elegoo™ was used as the separation film. The *Z*-stage of the building platform was driven stepper motor-powered linear stage with a 10 μm resolution (motorized Xslide™ XN150 Series Lead Screw from Velmex Inc., Bloomfield, NY).

2.3. Light intensity characterization

The light intensity of the LFV-VPP 3D printer was characterized using a charge-coupled device (CCD) camera and a light meter. A CCD camera mounted on the optical microscope (a pluggable 250× digital USB microscope) was used to measure the relative light intensity distribution of a single pixel of the LCD screen. Absolute light intensity measurements of the pixel were conducted using a digital handheld optical power and energy meter (PM100D, Thorlabs, Newton, NJ). A 30 μm pinhole (Precision Pinholes, Molybdenum Foils, Thorlabs, Newton, NJ) was placed over the light power meter to regulate incoming light spot size. A 150 μm thick FEP film was positioned on the LCD screen to simulate the printing setting during the light intensity measurements. The measurement results are presented in the Supplementary Information (Fig. S2). The 3D convoluted light intensity of the LCD mask images and the corresponding curing results were computed using MATLAB, based on the light intensity data from Fig. S2.

2.4. Feature roughness and dimension characterization

The roughness of the 3D-printed thin features was measured using an optical microscope (VHX-970f, Keyence, Itasca, Illinois) and processed with ImageJ software. The line roughness (Ra) was calculated using the equation: $\mathrm{Ra} = \frac{1}{L}\int_0^L |Z(x)|dx$. The line width was also measured using the optical microscope with an automatic edge detection function.

2.5. Fabrication and characterization of test cases

Honeycomb metamaterials and mesh filters were printed using the LFV-VPP 3D printer. The maximum strength and Young's modulus of the honeycomb metamaterials were measured using an F105-IMT Tensile Tester from MARK-10 Corp. (Copiague, NY). The force gauge was an M4-100 advanced digital force gauge series 4, also from Mark-10, with a maximum load capacity of 200 N. The filtering capability of the mesh filters was tested by pumping a mixture of water and microparticles through the 3D-printed mesh filters. The microparticle sizes vary from 75 μm to 300 μm. The printing parameters used in the test cases are shown in Table 1.

3. Results

3.1. LFV-VPP process design

Here, we use a honeycomb structure (Fig. 2a) as an example to demonstrate the developed LFV-VPP process. The computer-aided design (CAD) model of the honeycomb is sliced into layer mask images using commercial slicing software. After slicing, each layer mask image is divided into sub-mask images based on the direction of the line features in the sliced layer. All the line features in a sub-mask image are oriented in the same vibration direction (Fig. 2b). During the printing process of each layer, a multi-exposure approach is employed to print the linear features defined by each sub-mask image. The flow chart of the multi-exposure process (Fig. 2c) illustrates the printing cycle for a given layer. The LCD screen projects the first sub-mask image after the sub-mask images are generated from the layer mask image. Simultaneously, the piezo actuators generate a vibration motion along the direction of the feature using the first sub-mask image. Fig. 2d demonstrates how the piezo motions achieve feature-oriented vibration of sub-mask images 1, 2, and 3, respectively. Suppose n is the vibration steps (when $n = 1$ indicating no vibration), α is the vibration amplitude, and λ is the moving distance for each vibration step. Note the response time of the piezo stage is instantaneous (<1 μs) and can be omitted, so the delay time at each vibration step is $T_\lambda = \frac{T_{Exposure\ time}}{n \times 2}$. The second sub-mask image is loaded after exposing the first sub-mask image, and the corresponding piezo motion is planned. This process repeats until all the sub-mask images have been exposed. After all the sub-mask images of a layer have been exposed, the Z-stage moves upward to separate the built layers from the FEP film and then moves down to form a desired gap for building the next layer. The process repeats until all the layers have been built.

The feature-oriented vibration adjusts the light energy distribution of the photomask images, directly influencing the smoothness of the printed lines. We simulated the distribution of the accumulated light energy to assess the impact of controlled vibration. The accumulated light energy is calculated using the following equation, based on single-pixel light intensity calibration:

$$E(x,y) = \sum\nolimits_k I_k(x,y)t \tag{1}$$

Here, $E(x,y)$ represents the accumulated light energy, $I_k(x,y)$ is the intensity of light from a single pixel calibrated (refer to Fig. S2 in Support Information), and t is the exposure time.

To assess the effect of vibration, we calculated the accumulated light energy over the designed vibration using

$$E_v(x,y) = \sum_{i=0}^{n-1} E\left(x - \frac{i}{n}\alpha\cos\theta, y - \frac{i}{n}\alpha\sin\theta\right) \tag{2}$$

where $E_v(x,y)$ is the accumulated light energy after vibration, and θ is the vibration direction.

We then estimated the curing results using the accumulated light energy in the following photocuring model:

$$G(x,y) = \begin{cases} f(E_v(x,y)) \text{ if } f(E_v(x,y)) < d \\ d \text{ if } f(E_v(x,y)) \geq d \end{cases} \tag{3}$$

where d is the layer thickness, and f is the function relating light energy to curing depth that is calibrated, as shown in Fig. S1.

The light energy profiles of the vibrated sub-mask images 1, 2, and 3 are simulated and shown in Fig. 2e. The X and Y axes represent the position of the LCD screen, while the mesh plane depicts the curing threshold of the photocurable resin. From the light energy simulation, a smooth boundary for the linear features is observed in all the linear features. The magnified view of the curing result from the feature-oriented vibration method for a line $\theta = 30°$ shows a smooth boundary (Fig. 2e). In comparison, the simulated light energy profile of the same line using the feature-independent vibrational VPP [26] has a rough boundary (Fig. 2f). Using a vibration pattern of photomask images without considering the line angle θ, their simulated results for all the slope lines have more rugged boundaries than those of LFV-VPP, conforming to the experimental results (refer to Fig. 3l and m for line features with five different angles).

3.2. Vibration for improved line smoothness

In this section, we investigated the feature's smoothness related to the process parameters of LFV-VPP, focusing on thin lines oriented in arbitrary directions. The vibration amplitude, denoted as α, is defined as the distance between the initial and final positions of the mask image during vibration (Fig. 1i). It has a relation with pixel gap Δ by $\alpha = \frac{n-1}{n}\Delta$. For example, for LFV-VPP with vibration steps $n = 5$, the vibration amplitude to print a thin line feature in the $\theta = 0^\circ$ direction is α = 0.8× pixel size = 40 μm, if the pixel size is 50 μm. In each vibration step i, the LCD screen is moved forward by 10 μm (i = 0, 1, …, 4) and then backward (i = 4, 3, …, 0) (refer to Fig. 2d).

To illustrate this vibration amplitude's influences on the printed features' roughness, we conducted a detailed study using both simulations and physical experiments. We simulated the light energy distribution of the line feature mask images in LFV-VPP and the resulting photocuring behavior based on the energy distribution. As an example, we studied a thin-line feature in the $\theta = 0^\circ$ direction with a width of 150 μm. From the mask image of this line feature (Fig. 3a), we measured the corresponding light energy map (Fig. 3c). Using Eqs. (1) and (2), we modeled the light energy distribution in LFV-VPP at different vibration amplitudes α. The light energy distributions were demonstrated for vibration amplitudes of α = 0, 0.4×, 0.8×, 1.2× pixel sizes (Fig. 3b), where each pixel is 50 μm on the LCD screen used in this study. The curing results is simulated based on the light energy distribution and Eq. (3) (Fig. 3d). The results verified that the vibration amplitude at α = 0.8× pixel lengths improved energy uniformity. Further increasing α to 1.2× pixel lengths leads to non-uniformity of light energy distribution. This effect arises because the vibration overlaps with the neighboring pixels for the given n discrete piezo stopping points. When the vibration amplitude α = 0.8× pixel lengths for vibration steps $n = 5$, the shifted pixels were uniformly distributed between neighboring pixel gaps in the $\theta = 0^\circ$ direction. The roughness of the printed lines matches the uniformity of light energy.

Similarly, for a thin line feature in an arbitrary direction θ, the optimal vibration amplitude

Table 1
Printing parameters used in the test cases.

Test case	Layer thickness (μm)	Exposure time (s)	Pixel size (μm)
Thin line	50	3	50
Honeycomb	50	3	50
Mesh filter	25	1.7	50

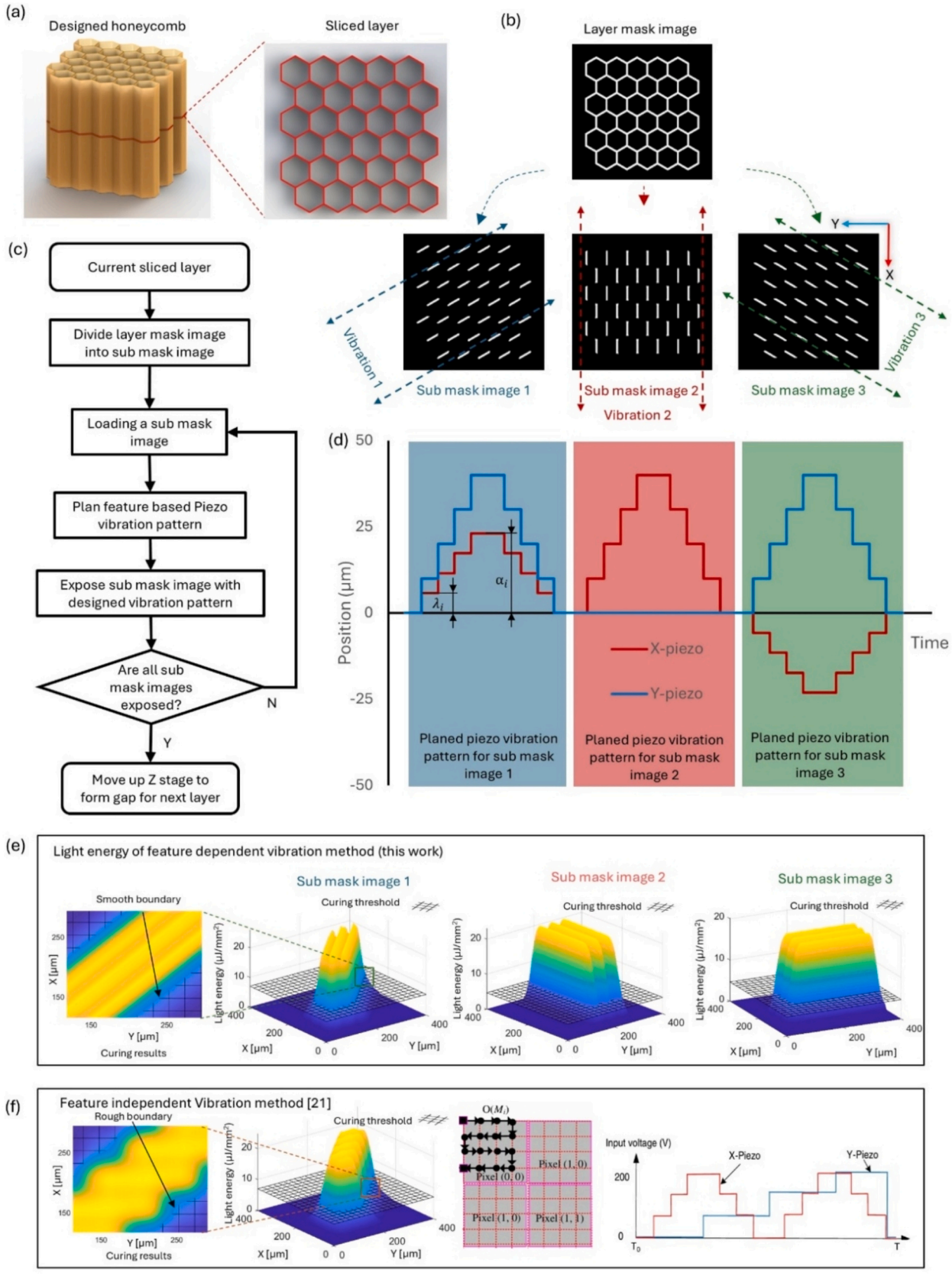

Fig. 2. Principle of the LFV-VPP process. (a) A CAD model of honeycomb; (b) generation of sub-mask images from the layer image; (c) flowchart of the LFV-VPP process to print one sliced layer; (d) motion planning of piezo actuators to generate linear vibration along the linear features' direction; (e) simulation of the accumulated light energy of the sub mask images printed by LFV-VPP; and (f) simulation of the accumulated light energy of the feature-independent vibrational VPP.

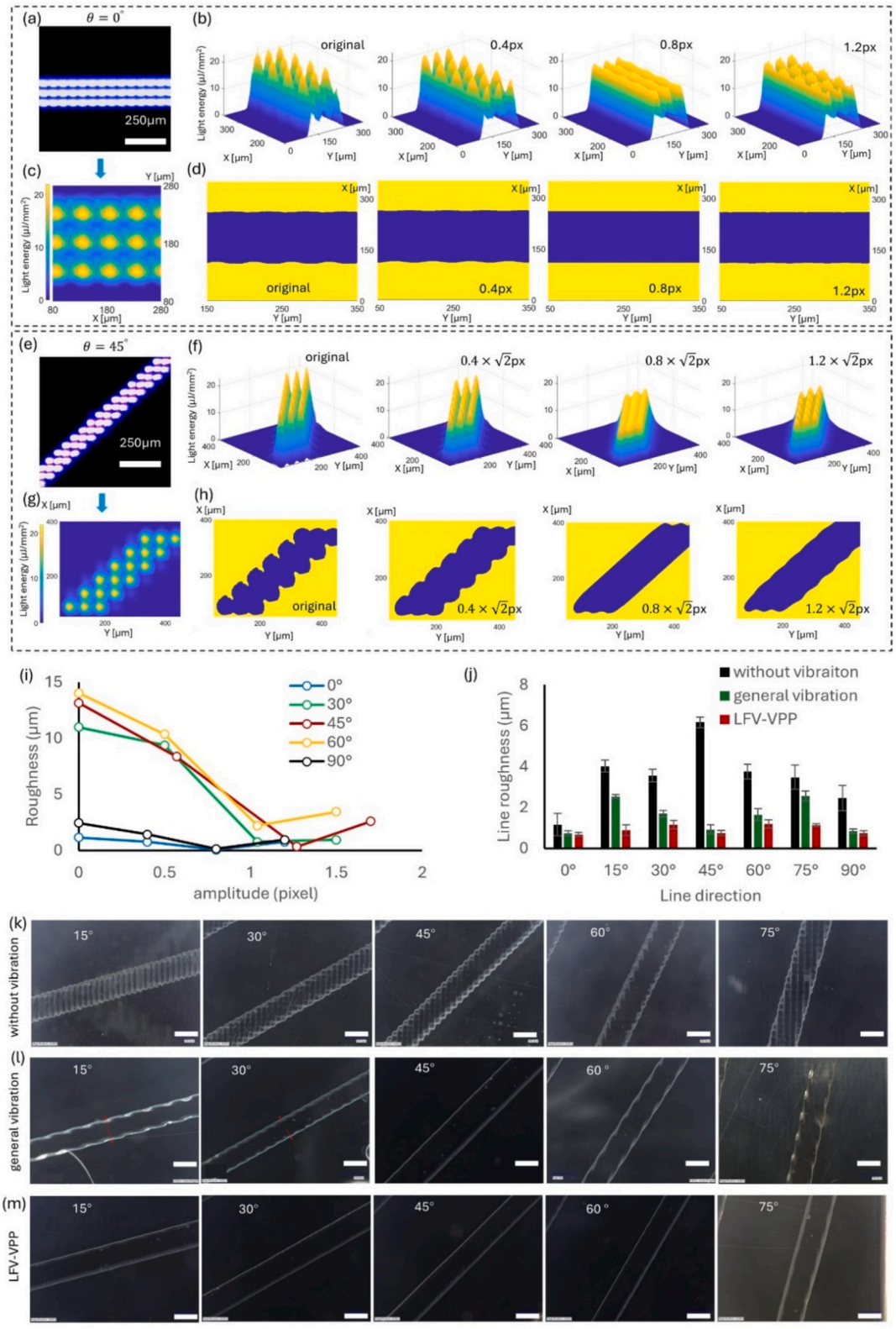

Fig. 3. Characterization of feature roughness printed by LFV-VPP. (a, c) Mask image of a line feature in the $\theta = 0^{\circ}$ direction; (b) simulated light energy distributions of the vibrational VPP for line features in the $\theta = 0^{\circ}$ direction; (d) simulated curing results of the vibrational VPP for line features in the $\theta = 0^{\circ}$ direction; (e, g) mask image of a line feature in the $\theta = 45^{\circ}$ direction; (f) simulated light energy distributions of the vibrational VPP for line features in the $\theta = 45^{\circ}$ direction; (h) simulated curing results of the vibrational VPP for line features in the $\theta = 45^{\circ}$ direction; (i) simulated roughness of line features printed with different vibration amplitudes; (j) experimental results of the roughness of line features in the $\theta = 0^{\circ}$–90° directions with and without LFV-VPP; (k) line features in the $\theta = 0^{\circ}$–90° direction printed by the commercial VPP (no vibration), scale bar: 200 μm; (l) line features in the $\theta = 0^{\circ}$–90° direction printed by feature-independent vibration, scalebar: 200 μm; and (m) line features in the $\theta = 0^{\circ}$–90° direction printed by LFV-VPP, scalebar: 200 μm.

$$\alpha = \Delta\left(1 - \frac{1}{n}\right) \tag{4}$$

where Δ is the pixel gap in the line direction, e.g., $\Delta = \sqrt{2}\times$ pixel size for $\theta = 45^{\circ}$. The smoothness of thin line features in such a direction can be further improved by combining the controlled vibration with grayscale mask images to define such line features. We demonstrated this by simulating the light energy distribution and the related curing results of a thin line in the $\theta = 45^{\circ}$ direction, using different vibration amplitudes. The physical mask image and the measured light energy map are shown in Fig. 3e and g. The grayscale values have been applied to the pixels on the boundary of the features using geometric heuristics [17,19]. The simulated light energy distributions show the light energy smoothness with the vibration along the $\theta = 45^{\circ}$ direction, with the amplitudes of $\alpha = 0$, $0.4\times\sqrt{2}$, $0.8\times\sqrt{2}$, $1.2\times\sqrt{2}$ pixel size (Fig. 3f). From the light energy distribution, we simulated the photocuring results of the lines in the $\theta = 45^{\circ}$ direction (Fig. 3h). The impact of vibration on the curing results for the lines is similar to that for the lines in $\theta = 0^{\circ}$ direction. The smallest feature roughness is achieved at $0.8\times\sqrt{2}$ pixel size vibration amplitude. This vibration can be achieved by synchronizing the piezo stages in the *X*- and *Y*- axes with vibration amplitudes $\alpha_x = \alpha\cos(45^{\circ})$ and $\alpha_y = \alpha\sin(45^{\circ})$. For LFV-VPP using different vibration amplitudes, the roughness of the line features in the $\theta = 0^{\circ}, 30^{\circ}, 45^{\circ}, 60^{\circ}$, and 90° directions are computed and shown in Fig. 3i, showing the vibration amplitude of $0.8\times\Delta$ leads to the smallest roughness.

Hence, the optimal vibration of LFV-VPP in the *X*- and *Y*- axes for a thin line feature in an arbitrary direction θ is set as:

$$\alpha_x = \Delta\cos(\theta)\left(1 - \frac{1}{n}\right); \alpha_y = \Delta\sin(\theta)\left(1 - \frac{1}{n}\right); \text{for } (0 \le \theta \le \pi) \tag{5}$$

This vibration amplitudes α_x and α_y equally distribute the light energy in each step of the photomask image between the gap of two neighboring pixels in the direction of vibration. The theoretical model shows the feature smoothness is not related to the vibration frequency, which has been verified experimentally (refer to Fig. S7).

We conducted physical experiments using LFV-VPP to print line features in the $\theta = 0^{\circ}$, $30^{\circ}, 45^{\circ}, 60^{\circ}$, and 90° directions based on Eq. (5) to verify the smoothness improvement. The commercial grayscale 3D printing results without vibration assistance are shown in Fig. 3k. Although the grayscale mask image reduces pixelated aliasing to less than one pixel size, the pixelated aliasing is still apparent. Fig. 3l shows the test results of the slope lines printed by the feature-independent vibration method [26]. The pixelated aliasing is reduced to a smaller waviness on the boundary while still visible. The LFV-VPP results (Fig. 3m) show a significant reduction of the feature roughness for all the lines. The average roughness of the printed thin line features using different VPP processes is shown in Fig. 3j. Slope lines without vibration exhibit the most prominent roughness, with measured R_a values ranging from 3.4 to 6.2 μm. The feature-independent vibration method has significant smoothness improvement for lines in $\theta = 0^{\circ}$ and 90° directions, while it is less effective in other line directions. In comparison, the average roughness using LFV-VPP is reduced to 0.7–1.2 μm for all the directions. These results demonstrate that LFV-VPP effectively improves a line's smoothness regardless of the line's direction.

3.3. Vibration for subpixel line width control

Pixelated aliasing on thin line features not only reduces line smoothness but also leads to variations in line width. Beyond enhancing boundary smoothness, LFV-VPP improves dimensional accuracy. By integrating grayscale mask images with feature-based vibration, subpixel-level control over line width can now be achieved. To control the line width, we first use a light energy distribution model to simulate the features' curing results. Then, we can reversely obtain the mask images needed to achieve the correct line width. Hence, the line width can now be fine-tuned to achieve subpixel precision by adjusting the grayscale values of the boundary pixels.

As an example, we simulated the accumulated light energy for thin line features in both $\theta = 0^{\circ}$ and $\theta = 90^{\circ}$ directions with a 5-pixel width, printed by LFV-VPP. Grayscale values of 0 (completely dark), 150, and 255 (completely white) were applied to the rightmost column of pixels for the lines in the $\theta = 0^{\circ}$ direction and the topmost row for the lines in the $\theta = 90^{\circ}$ direction, respectively. The accumulated light energy and the resulting curing widths are plotted in Fig. 4a and b. The simulated photocuring results indicate a reduction in line width as the grayscale value decreased. From the simulation, we can build a relationship between the grayscale value and the line width (Fig. 4g). Noticeably, the curing results in the $\theta = 90^{\circ}$ direction were approximately 10 μm wider than the $\theta = 0^{\circ}$ directional line at the same grayscale level due to the asymmetric shape of the photomask image pixels in LCD-VPP (refer to Fig. 3a and c).

We conducted physical printing tests of the line width control to verify the simulation results. The mask images used in the physical testing experiments are shown in Fig. 4c, with six different grayscale levels of 0, 50, 100, 150, 200, and 255 applied to the rightmost pixel of the line features. The experimental results match well with the simulation results. Fig. 4d shows the printed results without vibration, where pixelated structures resembling spikes are visible on the lines, particularly in the segments where grayscale was applied, since the reduced light energy at the grayscale pixels exacerbates the pixels' non-uniform light distribution (Fig. 4f). After applying vibration, the printed results in Fig. 4e exhibit smooth boundaries, and the line width gradually decreases as the pixels' grayscale value is reduced. The relationship between the line width and the grayscale value corresponds well between the simulation and physical experiments, as shown in Fig. 4g. We can use the simulated curing results to determine the necessary grayscale values for the desired line width. This line width control method can also be applied to slope lines.

The LFV-VPP process can provide subpixel-level dimensional accuracy control. We printed slope lines with $\theta = 30^{\circ}$, 45°, and 60° angles to verify the control of subpixel-level dimensional accuracy. The printed results are shown in Fig. S4a–c. For each direction, we printed three target line widths of 200 μm, 220 μm, and 240 μm. The experiment results demonstrate an error of <7.4 μm compared to the designed line widths (refer to Fig. 4h). This line width control method can also improve the dimensional accuracy of a gap between neighboring line features. We performed a verification case for controlled line gaps by printing lines in the $\theta = 0^{\circ}$ and $\theta = 90^{\circ}$ directions with target gap widths of 170 μm and 340 μm, respectively (refer to Fig. S4d–g in Support Information). The printed line gap achieved <4.5 μm error compared to the design targets (Fig. 4i). Compared to a pixel size of 50 μm, LFV-VPP can achieve sub-pixel dimensional control for both line width and line gaps. Two test cases are designed to demonstrate this dimensional control capability. They are presented in the following sections to demonstrate the potential benefits enabled by LFV-VPP.

3.4. Demonstration of LFV-VPP on improved line smoothness and dimensional accuracy

We use a honeycomb structural material as a test case to illustrate the benefits of LFV-VPP with improved surface smoothness. Honeycomb structures are characterized by their hexagonal cells, which offer efficient material use and a high strength-to-weight ratio [28,29]. These properties make honeycomb structures widely adopted across multiple industries, including impact absorption [30], thermal insulation [31], and lightweight core panels [32]. The macroscopic transverse strength of the honeycomb structure is primarily determined by the strength of the walls in each honeycomb cell [33]. Smooth cell walls with less pixelated aliasing can result in a stronger honeycomb structure by reducing stress concentration at these non-smooth locations. Hence, the

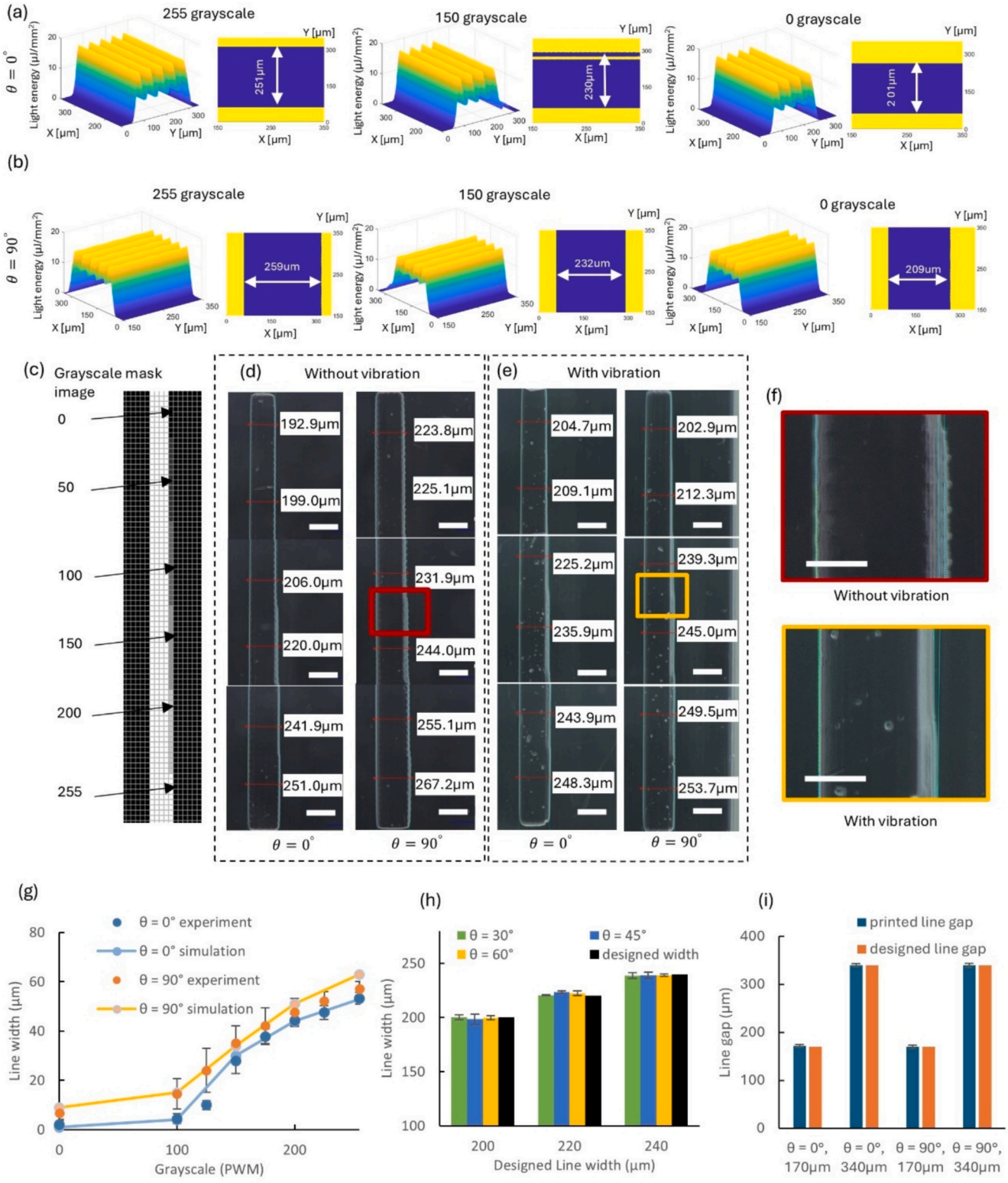

Fig. 4. Subpixel-level line width control using LFV-VPP combined with grayscale mask images. (a, b) The simulated line width of the thin line features printed by LFV-VPP with grayscale mask images in the $\theta = 0^{\circ}$ and $\theta = 90^{\circ}$ directions; (c) grayscale mask images of thin line features; (d) printing results of thin line features using commercial VPP, scalebar: 200 μm; (e) printing results of thin line features by LFV-VPP, scale bar: 200 μm; (f) comparison of the printing results of commercial VPP and LFV-VPP, scale bar: 100 μm; (g) simulated and experimental line width vs. grayscale value; (h) line width accuracy study of slope lines; and (i) line gap accuracy study.

3D-printed cell walls have an improved overall strength (refer to Video S1).

To highlight the benefits of LFV-VPP in producing smooth line features, we designed and fabricated a honeycomb cube with a wall thickness of 150 μm using conventional LCD-VPP and LFV-VPP. The designed model of the honeycomb structure is shown in Fig. 5a. Fig. 5b–d present the results from conventional LCD-VPP, where the magnified image of a single honeycomb cell reveals zigzag textures on each wall. The uneven line width leads to stress concentration under external loads, compromising the structural integrity. In contrast, Fig. 5e illustrates the approach adopted in LFV-VPP. The mask image of each layer was split into three sub-images, marked in red, yellow, and blue, with lines in the same color having the same vibration direction. These sub-images were sequentially printed with the corresponding vibration directions. The detailed printing process is shown in Fig. 2c and d. The printing results using LFV-VPP are shown in Fig. 5f–h. The significant reduction in pixelated aliasing leads to uniform wall thickness, eliminating stress concentration points and thereby increasing the maximum strength of the honeycomb structure using the same amount of material.

We performed compression testing to verify the strength

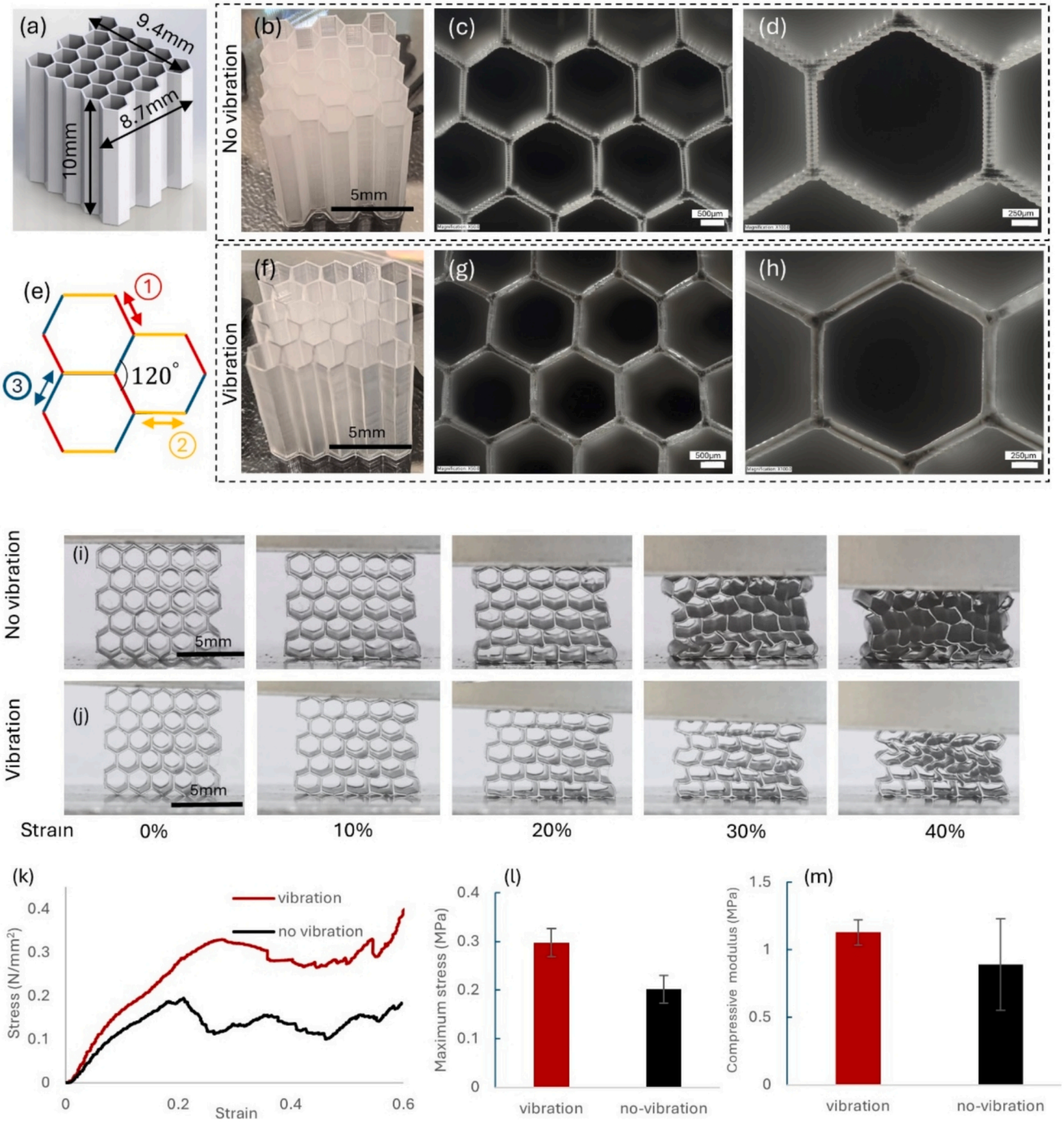

Fig. 5. Honeycomb structures are printed using regular LCD-VPP and LFV-VPP printers. (a) The CAD design of a honeycomb structure; (b–d) 3D-printed honeycomb structure using LCD-VPP without vibration; (e) multi-exposure of the honeycomb mask image using LFV-VPP; (f–h) 3D-printed honeycomb structure using LFV-VPP; (i–j) compressive testing of the 3D-printed honeycomb structures; (k) stress-strain plots from the compressive tests; (l) maximum compressive strength of the 3D-printed honeycomb structures; and (m) compressive modulus of the 3D-printed honeycomb structures.

improvement of the honeycomb structure. Fig. 5i and j show that, as the strain increases, the non-vibrate-printed honeycomb buckles at 20 % strain, whereas the LFV-VPP-printed honeycomb buckles until 30 % strain. The stress vs. strain plot is shown in Fig. 5k, where the LFV-VPP-printed honeycomb exhibits higher stress at the same strain and a higher maximum stress than the non-vibrate-printed honeycomb. Repeated experiments confirmed these results, with the average maximum strength shown in Fig. 5l. The maximum strength of the honeycomb printed by LFV-VPP was 50 % higher than that of the non-vibrate-printed honeycomb. Additionally, the LFV-VPP-printed honeycomb is stiffer, as evidenced by a 25 % higher compressive modulus with a smaller variation during the elastic deformation (Fig. 5m), mainly due to the reduced stress concentration on its side walls. This test case demonstrates the importance of addressing the stress concentration defects due to pixelated aliasing in the LCD-based VPP. With improved feature smoothness with fewer such defects, LFV-VPP can improve cellular structures' mechanical properties for various applications.

3.5. Demonstration of LFV-VPP on subpixel line gap control

We designed and tested a 3D-printed mesh filter of micro-particles to test LFV-VPP's subpixel-level dimensional accuracy control. Fig. 6a shows a mesh printed without vibration, where mesh size is uncontrollable at the subpixel level. In contrast, the LFV-VPP printed mesh with well-controlled mesh sizes (in 10 μm increments for a pixel size of 50 μm). Fig. 6e shows the design of a mesh filter, in which an inlet nozzle is at the top, and a 3 × 3 array of meshes is at the bottom. The 3D-printed mesh filter is shown in Fig. 6f, with its cross-sectional views at the *A-A* plane shown in Fig. 6g. The 3D-printed mesh filter can have designed gap sizes to filter micro-particles with different sizes. The magnified views of three meshes, in which the mesh sizes of the 3D-printed filters were designed to be 120 μm, 100 μm, and 70 μm, respectively, are shown in Fig. 6h–j, to highlight the subpixel-level control of LFV-VPP in printing mesh filters.

A particle filtering experiment was conducted to test the filtering capability of the 3D-printed mesh filters (Fig. 6d). Microparticles ranging from 75 μm to 300 μm were mixed with water and poured into the filters (Fig. 6b and c). The process is also shown in Video S2. Fig. 6k displays the particles before and after filtering, where the clarity of the water improves as the mesh size decreases. After passing through the mesh filter with a 120 μm mesh size, particles larger than 120 μm were filtered out, as shown in Fig. 6l. After passing through the mesh filter with a 70 μm mesh size, nearly all particles were filtered out (Fig. 6m). In addition to mesh filters with regular patterns, we further printed a mesh filter with a different mesh pattern in the shape of the USC logo (Fig. 6n) to demonstrate LFV-VPP's capability in fabricating highly customized mesh filter designs. As shown in Fig. 6o and p, LFV-VPP reduces the pixelated aliasing on all the walls in $\theta = 0^{\circ}$, 45° and 90° directions, allowing for accurate gap control to better control the microparticle sizes that can pass through the mesh filters.

4. Discussion

Pixelated aliasing has been a persistent challenge in line printing since the advent of mask image projection-based vat photopolymerization. Previous approaches developed to reduce pixelated aliasing in DMD- and LCD-VPP primarily rely on planning mask images with grayscale pixels to adjust the input light energy to control the photocuring results. However, grayscale mask images cannot effectively remove pixelated aliasing in LCD-VPP. As illustrated in cases i and ii, only changing the energy level of pixels is insufficient to achieve a smooth boundary on the printed lines (Fig. 7a–c). For LCD-VPP, grayscale pixels even make pixelated aliasing more severe because of the lack of pixel blending between neighboring pixels in LCD-VPP. The reduced light intensity of a grayscale pixel on the boundary leads to insufficient photocuring energy in the gap between two neighboring pixels.

The vibration-assisted VPP process [26] utilized a general vibration method to blend the energy of a pixel and its neighbors (case iii), achieving improved feature smoothness compared to LCD-VPP without vibration. However, this feature-independent vibration process still causes waviness on the printed slope lines with angles other than $\theta = 0^{\circ}$ and $\theta = 90^{\circ}$ (Fig. 7c-iii). The key advantage of LFV-VPP is that it introduces a feature-oriented vibration to achieve uniform light energy between the neighboring pixels of a line feature, so the feature's pixelated aliasing can be effectively eliminated with accurate dimension control (Fig. 7c-iv). Our findings indicate that LFV-VPP allows for 1.5 μm line smoothness and 10 μm dimensional accuracy for a pixel size of 50 μm, surpassing the precision achieved with grayscale mask images and feature-independent vibration-assisted VPP. This approach is particularly suitable for fabricating thin line features that require both smoothness and dimensional accuracy at the microscale.

The simulation of the $\theta = 0^{\circ}$ directional line at the grayscale level of 150 predicts an uncured slit (Fig. 4a) because the reduced light intensity of grayscale pixels on the boundary leads to insufficient photocuring energy between the neighboring pixels. We further illustrate this phenomenon in Fig. 7d. When the grayscale level 150 is applied to the boundary pixels, the pixels' energy level is reduced in the LCD photomask. Accordingly, the accumulated energy of all the pixels forms a valley on which the light energy level is lower than the curing threshold. The slit is small and was not observed in the experimental results (Fig. 7d-iv). This discrepancy may be due to the scattering of the UV light by the FEP film, so the accumulated light energy on the boundary cures the small gap portion between the slit lines.

The developed LFV-VPP process only requires a small vibration amplitude (<50 μm in the *X*- and *Y*-axes). Such a small vibration amplitude is unnoticeable to humans in the fabrication process, but it can effectively achieve uniform light intensity distribution along line features. Despite its advantages, LFV-VPP uses a multi-exposure strategy to fabricate lines in each direction sequentially. Hence, it reduces fabrication speed for a design with line features in multiple directions and could be time-consuming for layers with complex thin line features. To address the trade-off between reduced fabrication speed and improved line smoothness and accuracy, this multi-exposure method may be applied only to critical features, such as controlled line gaps and critical mating surfaces. For example, for the model shown in Fig. 6e, we used LFV-VPP to fabricate 10 layers related to the mesh filters, and all the other layers (390 layers) were printed using the regular LCD-VPP process without vibration. Accordingly, the total building time of the model for a commercial LCD-VPP printer (without vibration) and the LFV-VPP printer (with vibration for 10 layers) are 26.33 min and 26.67 min, respectively. The fabrication speed difference is less than ~1.3 % for the mesh filter test cases.

5. Conclusion

This study presents a novel feature-oriented vibration method in LCD-based vat photopolymerization to achieve sub-pixel precision in printing line features with smooth boundaries and accurate dimensions. The approach eliminates pixelated aliasing without introducing dimensional errors, enabling a line smoothness of 1.5 μm and dimensional accuracy of 10 μm for LCD photomasks with 50 μm pixel size. The method's effectiveness was validated by successfully fabricating honeycomb structures and mesh filters, demonstrating its capability to produce thin wall structures free from pixelation defects. These results highlight the potential of the LFV-VPP technique to enhance the quality and precision of LCD-based VPP for intricate geometries at the microscale. Beyond the tested applications, the LFV-VPP method shows promise for broader use in microstructure fabrication and microfluidic systems [34].

Our study establishes the foundational principle of vibration-assisted VPP, offering a robust basis for advancing this additive manufacturing technique toward high-precision fabrication. The proposed feature-

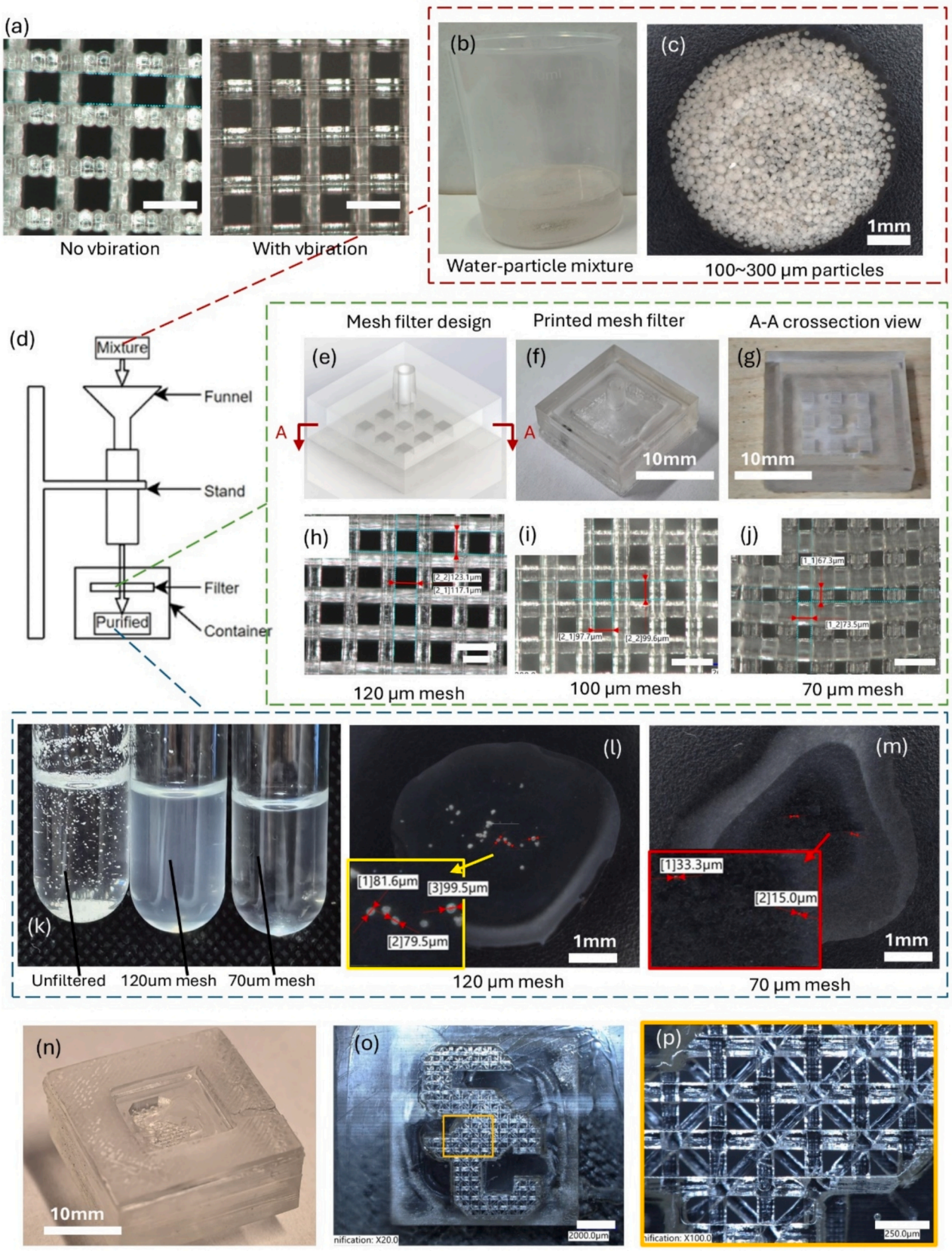

Fig. 6. The LFV-VPP printed mesh filters. (a) Comparison of the meshes in the filter printed using commercial LCD-VPP and LFV-VPP printers, scale bar: 200 μm; (b, c) unfiltered water-particle mixture used in the filtering test; (c) the schematics of the particle filtering test; (e) the CAD model of the 3D-printed mesh filter; (f) the printed mesh filter by LFV-VPP; (g) cross-sectional views of the mesh filter at the *A-A* plane. (h–j) Meshes sizes in the LFV-VPP printed filters, scale bar: 200 μm; (k) water-particle mixtures before and after filtering; (l, m) filtered particles after passing through mesh filters with 120 μm and 70 μm mesh sizes; (n) 3D-printed customized mesh filter with the 'USC' logo pattern; and (o, p) customized mesh pattern in the shape of the USC logo printed by LFV-VPP.

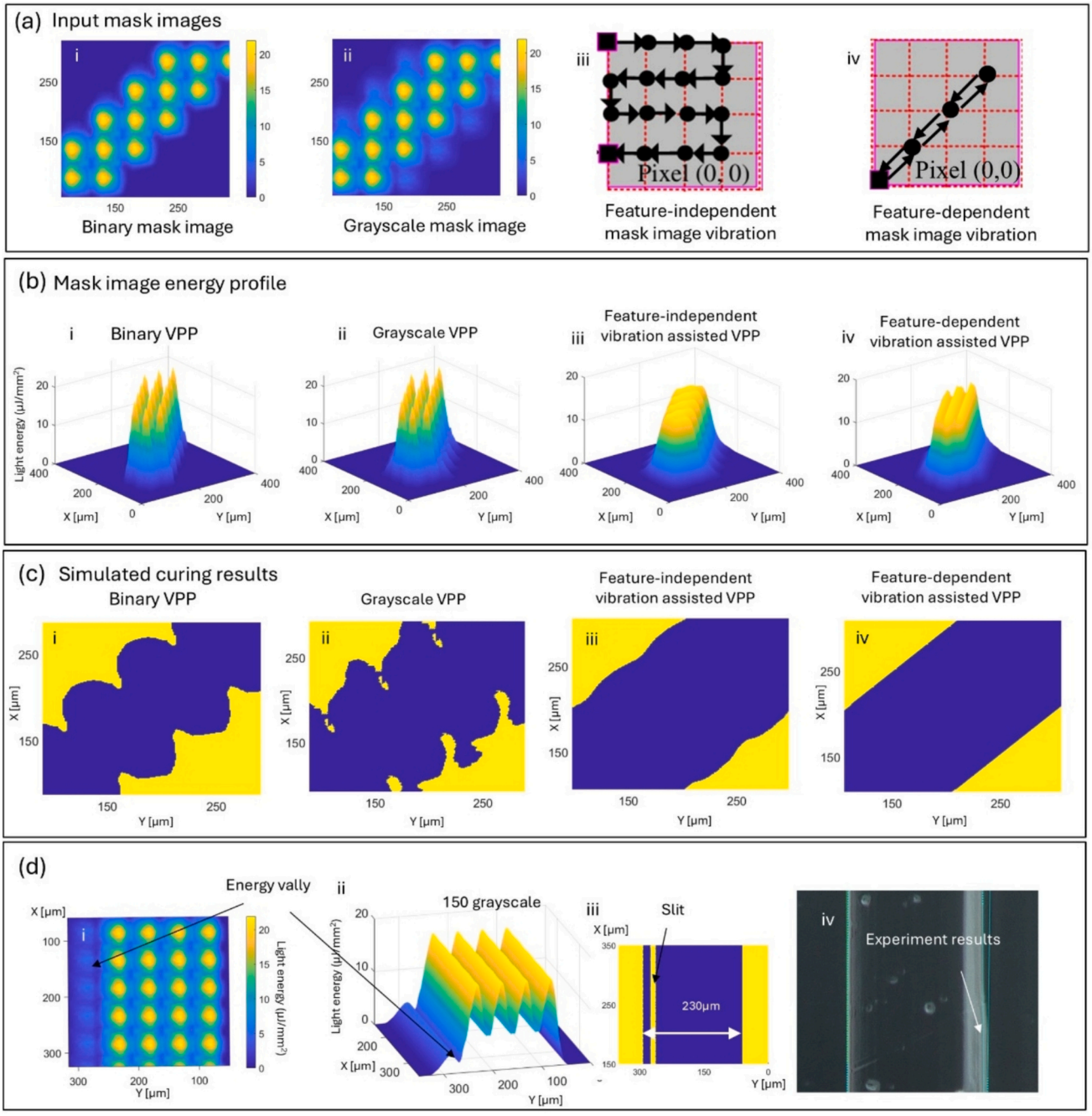

Fig. 7. Discussion and analysis of LFV-VPP. (a) Input mask images of different VPP processes; (b) a comparison of the mask image energy profile of the LCD-VPP and LFV-VPP processes; (c) a comparison of the curing results of the LCD-VPP and LFV-VPP processes; and (d) study of the "slit" in the simulated curing results.

oriented vibration method is currently limited to line feature fabrication. Curved contours must first be approximated as polylines before line-based vibration patterns are applied segment by segment. Future research should investigate more advanced vibration strategies that enable direct fabrication of curved geometries without approximation. We hope this work will inspire further systematic studies to extend vibration-assisted VPP to more complex and general feature geometries.

Supplementary data to this article can be found online at https://doi.org/10.1016/j.jmapro.2025.05.034.

CRediT authorship contribution statement

Han Xu: Writing – review & editing, Writing – original draft, Visualization, Validation, Software, Methodology, Formal analysis, Data curation. **Qizhou Li:** Validation, Investigation. **Shangxiong Zhang:** Visualization, Investigation, Formal analysis. **Changyuan Pu:** Investigation, Formal analysis, Data curation. **Yizhu Chen:** Investigation, Formal analysis. **Yong Chen:** Writing – review & editing, Supervision, Resources, Project administration, Methodology, Funding acquisition, Conceptualization.

Declaration of competing interest

The authors declare that they have no known competing financial interests or personal relationships that could have appeared to influence the work reported in this paper.

Acknowledgments

The authors acknowledge the help of Dr. Huachao Mao and Mr. Shutao Cai at USC's CAM, who built the piezo-driven linear stage used in the study. The authors also acknowledge Professor Hangbo Zhao at USC for his help with compression tests.

References

[1] Sjölund J, Karakoç A, Freund J. Effect of cell geometry and material properties on wood rigidity. Int. J. Solids Struct. 2015/06/01;62:207–16. https://doi.org/10.1016/j.ijsolstr.2015.02.029.
[2] Shah M, et al. Vat photopolymerization-based 3D printing of polymer nanocomposites: current trends and applications. RSC Adv. 2023;13(2):1456–96.
[3] Huang J, Qin Q, Wang J. A review of stereolithography: processes and systems. Processes 2020;8(9):1138.
[4] Haldar B. Enhancing dimensional accuracy in budget-friendly 3D printing through solid model geometry tuning and its use in rapid casting. Machines 2023;11(11):1020.
[5] Pan Y, Zhou C, Chen Y. A fast mask projection stereolithography process for fabricating digital models in minutes. 2012.
[6] Paral SK, Lin D-Z, Cheng Y-L, Lin S-C, Jeng J-Y. A review of critical issues in high-speed vat photopolymerization. Polymers 2023;15(12):2716.
[7] Li Y, et al. Strontium-doped calcium silicate scaffolds with enhanced mechanical properties and tunable biodegradability fabricated by vat photopolymerization. Int J Bioprint 2023;9(6):1233.
[8] Moharana AP, Raj R, Dixit AR. Fabrication of continuous woven E-glass fiber composite using vat photopolymerization additive manufacturing process. Rapid Prototyp. J. 2024;30(2):253–69.
[9] Li X, et al. 3D printing of hydroxyapatite/tricalcium phosphate scaffold with hierarchical porous structure for bone regeneration. Bio-Des. Manuf. 2020;3:15–29.
[10] Ribeiro N, Nunes CMM, Rodrigues AFM, Sousa A, Olhero SM. Toughening robocast chitosan/biphasic calcium phosphate composite scaffolds with silk fibroin: tuning printable inks and scaffold structure for bone regeneration. Biomater Adv 2022;134:112690.
[11] Li X, Xie B, Jin J, Chai Y, Chen Y. 3D printing temporary crown and bridge by temperature controlled mask image projection stereolithography. Procedia Manuf 2018;26:1023–33.
[12] Son K, Lee J-H, Lee K-B. Comparison of intaglio surface trueness of interim dental crowns fabricated with SLA 3D printing, DLP 3D printing, and milling technologies. 2021, vol. 9: MDPI, 8 ed., p. 983. Healthcare (Basel) 2021;9(8):983. https://doi.org/10.3390/healthcare9080983.
[13] Bodaghi M, Damanpack AR, Hu GF, Liao WH. Large deformations of soft metamaterials fabricated by 3D printing. Mater. Des. 2017;131:81–91.
[14] Zhang KP, et al. 3D printed embedded metamaterials. Small 2021;17(50):2103262.
[15] Quan H, Zhang T, Xu H, Luo S, Nie J, Zhu X. Photo-curing 3D printing technique and its challenges. Bioact Mater 2020;5(1):110–5.
[16] Prabhakar MM, Saravanan AK, Lenin AH, Mayandi K, Ramalingam PS. A short review on 3D printing methods, process parameters and materials. Mater Today Proc 2021;45:6108–14.
[17] Zhou C, Chen Y. Additive manufacturing based on optimized mask video projection for improved accuracy and resolution. J. Manuf. Process. 2012;14(2):107–18.
[18] Shan Y, Krishnakumar A, Qin Z, Mao H. Reducing lateral stair-stepping defects in liquid crystal display-based vat photopolymerization by defocusing the image pattern. Addit Manuf 2022;52:102653.
[19] Zhou C, Chen Y, Waltz RA. Optimized mask image projection for solid freeform fabrication 2009;49026:543–57.
[20] Sun C, Fang N, Wu DM, Zhang X. Projection micro-stereolithography using digital micro-mirror dynamic mask. Sensors Actuators A Phys. 2005;121(1):113–20.
[21] Xu H, et al. Continuous vat photopolymerization for optical lens fabrication. Small 2023;19(40):2300517.
[22] Zheng X, et al. Ultralight, ultrastiff mechanical metamaterials. Science 2014;344(6190):1373–7.
[23] Zhou C, Xu H, Chen Y. Spatiotemporal projection-based additive manufacturing: a data-driven image planning method for subpixel shifting in a split second. Adv. Intell. Syst. 2021;3(12):2100079.
[24] Yuan C, et al. Ultrafast three-dimensional printing of optically smooth microlens arrays by oscillation-assisted digital light processing. ACS Appl. Mater. Interfaces 2019;11(43):40662–8.
[25] Zhou C, Chen Y. Additive manufacturing based on multiple calibrated projectors and its mask image planning 2010;44090:439–49.
[26] Xu H, Hu R, Chen S, Zhu J, Zhou C, Chen Y. Vibration-assisted vat photopolymerization for pixelated-aliasing-free surface fabrication. Int J Extreme Manuf 2024;6(3):035004.
[27] Anycubic. "Standar Resin 1KG Clear Resin Parameters." https://store.anycubic.com/products/colored-uv-resin (accessed.
[28] Vaziri A, Hutchinson JW. Metal sandwich plates subject to intense air shocks. Int. J. Solids Struct. 2007;44(6):2021–35.
[29] Yuan Y, et al. Lightweight, thermally insulating and stiff carbon honeycomb-induced graphene composite foams with a horizontal laminated structure for electromagnetic interference shielding. Carbon 2017;123:223–32.
[30] Xiang J, Du J. Energy absorption characteristics of bio-inspired honeycomb structure under axial impact loading. Mater. Sci. Eng. A 2017;696:283–9.
[31] Yang C, et al. High thermal insulation and compressive strength polypropylene microcellular foams with honeycomb structure. Polym. Degrad. Stab. 2021;183:109406.
[32] Du Y, Yan N, Kortschot MT. Light-weight honeycomb core sandwich panels containing biofiber-reinforced thermoset polymer composite skins: fabrication and evaluation. Compos Part B Eng 2012;43(7):2875–82.
[33] Ajdari A, Jahromi BH, Papadopoulos J, Nayeb-Hashemi H, Vaziri A. Hierarchical honeycombs with tailorable properties. Int. J. Solids Struct. 2012;49(11–12):1413–9.
[34] Xu Y, et al. In-situ transfer vat photopolymerization for transparent microfluidic device fabrication. Nat. Commun. 2022;13(1):918.